



Trans. Nonferrous Met. Soc. China 35(2025) 3218-3239

Transactions of Nonferrous Metals Society of China

www.tnmsc.cn



Texture evolution in extrusion and rolling processes of 2195 Al–Li alloy

Yong-xiao WANG^{1,2}, Yang FU¹, Xiao XU³, Hui LI¹, Wen-dong ZHANG⁴, Rui FENG¹, Yao-kun PAN¹, Xiao-li CUI¹

- 1. School of Materials Science and Engineering, Shandong University of Technology, Zibo 255000, China;
 - 2. Shandong Nanshan Aluminum Co., Ltd., Longkou 265700, China;
 - 3. College of Machine, Shanghai Dianji University, Shanghai 201306, China;
 - 4. Linqu Inspection and Testing Center, Linqu 262600, China

Received 20 February 2024; accepted 30 October 2024

Abstract: The microstructure and texture evolutions during extrusion and rolling processes of the 2195 Al–Li alloy were investigated. The EBSD technique was employed to reveal the microscopic evolution mechanisms of different texture components. The findings reveal that the texture evolution is governed by two mechanisms: an overall orientation transformation induced by plastic strain and a localized transformation occurring at the shearing bands within grains. During the rolling process, the extrusion texture components of Ex $\{123\}\langle 111\rangle$ and Cu $\{112\}\langle 111\rangle$ evolve into S $\{123\}\langle 634\rangle$, and the Bs $\{011\}\langle 211\rangle$ rotates into the orientations near R-Bs and S. With increasing deformation, the S, Bs, and R-Bs orientations further rotate around the TD axis and disperse into new orientations, forming recrystallized grains. The shearing bands with different initial orientations exhibit similar orientation evolution patterns, all of which evolve from the initial orientation to a series of recrystallization orientations.

Key words: Al-Li alloy; texture evolution; grain orientation; extrusion and rolling processes; microstructure

1 Introduction

Compared with the conventional aerospace aluminum alloys, such as the 2xxx and 7xxx series, third-generation of Al–Li alloys exhibits a lower density, a higher elastic modulus, and superior specific strength and stiffness [1,2]. The addition of 1 wt.% Li to Al can decrease the density by 3% and increase the stiffness by 6% [3]. Moreover, the presence of Li promotes precipitation and improves the fatigue resistance and damage tolerance of the alloy [4]. Therefore, Al–Li alloys have found increasing use in the aerospace industry, including aircraft fuselage skins and stringers, launch vehicle fuel tanks, and structural parts for spacecraft resource storage [5]. Since these components are

commonly used, understanding the evolution of microstructures during thermoplastic-forming of the components is crucial, as it directly affects the final mechanical properties.

It is widely known that strong crystallographic textures are often formed in Al–Li alloy parts. These texture components significantly impact the static strength, dynamic fatigue performance, anisotropy of mechanical properties, and corrosion resistance [6–8]. The formation and evolution of textures are closely associated with deformation temperature, strain type and level experienced by the billet. Aluminum-based alloys tend to develop $\langle 111 \rangle$ and $\langle 100 \rangle$ fiber textures during the extrusion process because of triaxle compressive stress, whereas β -fiber textures are often formed in rolling plates [9–11]. The texture components involved in

the β -fiber are relatively uniform under cold rolling, whereas the Bs component increases substantially during hot rolling [6]. MAURICE and DRIVER [12] and VATNE et al [13] reported that the Bs component contains fewer substructures and has lower stored energy, which prevails for deformation conditions at low strain rates and high temperatures. Additionally, texture evolution can be altered significantly by shear strain, which is often introduced through multidirectional forging or asymmetric rolling [14,15]. A strong shear strain weakens deformation textures, Bs $\{011\}\langle 211\rangle$, S $\{123\}\langle 634\rangle$, and Cu $\{112\}\langle 111\rangle$, and transforms them into γ -fiber and R-Cube textures. Such texture modifications are believed to increase the Lankford parameter of the plate, thus improving formability [16]. In addition to the deformation parameters, the texture evolution is also dependent on the initial grain orientation and composition [17-19]. For Cube-oriented grains are inclined to form the S orientation during rolling, whereas grains with an R-Cube orientation tend to transform into Cu orientation [20,21]. The Goss orientation may rotate into the Bs texture or remain unchanged under different deformation conditions [22]. However, the above evolution rules have exceptions for different alloys and deformation conditions. RAABE et al [23], and LIU and MORRIS [24] reported that the Cube orientation could transform into Bs via α -fiber or R-Cube.

The texture evolution in terms of microscopic view is governed by shearing bands, grain rotation, and recrystallization behavior during deformation. The microstructure of Al-Li alloys varies when subjected to different deformation conditions. The shearing bands are more prominent during deformation at low temperatures and high strain rates, whereas recrystallization is inhibited [25,26]. The dislocations tend to annihilate through recovery and recrystallization at high temperatures and low strain rates [27]. In many cases, these two mechanisms coexist, and the grain orientation transformation occurs simultaneously in diverse ways. At present, the effects of deformation parameters on the overall texture and mechanical properties of Al-Cu-Li alloys have attracted considerable attention [11,28,29]. However, there is a notable lack of specific information regarding the micro-mechanisms of the grain orientation transformation during extrusion and rolling processes, which is essential for predicting and controlling texture components. Moreover, the formation of recrystallized grains and special grain boundaries is also closely related to the orientation transformation process, which is fundamental for refining grains and suppressing abnormal coarsening.

In this study, the microstructure and texture evolution behaviors are examined during the extrusion and rolling processes of 2195 alloy via electron backscatter diffraction (EBSD) characterization and analysis. Specifically, the micro-mechanisms underlying the evolution of various initial texture components are elucidated. These findings provide theoretical guidance for predicting and controlling texture in the thermoplastic forming process of Al–Cu–Li alloys. Furthermore, this work also provides valuable assistance for in-depth research on abnormal grain growth during thermal deformation and heat treatment.

2 Experimental

2.1 Processing methods

The chemical composition of the as-cast 2195 alloy is Al-4.08Cu-1.06Li-0.51Mg-0.35Ag-0.09Zr (wt.%). First, the as-cast billet was homogenized at 500 °C for 24 h to eliminate segregation defects and enhance microstructure uniformity. After homogenization, the billet was air cooled to room temperature. The homogenized billets with a size of d120 mm × 370 mm were subsequently preheated to 470 °C and subjected to hot extrusion on an 800 T extruder. The rod speed was set as 1.0 mm/s. The extrusion cylinder diameter was 125 mm, and the extrusion ratio was therefore 25:1. After the extrusion process, a plate with a cross-sectional size of 60 mm × 8 mm was produced.

To conduct the rolling experiments, the extruded plate was first cut to a length of 100 mm. The plates were preheated at 460 °C for 20 min to ensure uniform heating. Several rolling experiments were carried out to obtain the rolled plates with different thicknesses. Table 1 lists the processing parameters and their corresponding labels for each experiment. Thin plates required multiple rolling passes due to the large reduction in thickness. To

Table 1 Experimental process parameters

| Table 1 | Experimental proc | cos parameters | | |
|---------------------|-----------------------------------|--------------------------------------------------------------------------|-------------------------------|--|
| Label | Processing technology | Rolling reduction/mm | Rolling temperature/ °C | |
| EX | Extrusion | - | _ | |
| SR ₄₆₀₋₆ | Extrusion and synchronous rolling | 2 (Single pass) | 460 | |
| SR ₄₆₀₋₄ | Extrusion and synchronous rolling | 4 (Two passes) | 460 | |
| SR ₄₆₀₋₂ | Extrusion and synchronous rolling | 6 (Three passes) | 460 | |
| SR ₄₆₀₋₁ | Extrusion and synchronous rolling | 7 (Four passes) | 460 | |
| DSR | Extrusion and asymmetric rolling | 6 (Three passes with different speed ratios of 1:1.2 and 1:1.6) | 460 | |

maintain the rolling temperature, a heating treatment at 460 °C for 5 min was applied before each rolling pass. The asymmetric rolling experiments were also carried out to obtain the rolled plates with shear deformation. Aside from different roller speeds, all the other experimental conditions of asymmetric rolling remained consistent with those of symmetric rolling. The extrusion direction (ED) of the plates was set as the rolling direction. To provide a clear depiction of the experimental procedures, Fig. 1 presents a diagram illustrating the processing route.

2.2 Sampling and characterization methods

To study the microstructure of plate with different processes, samples were cut for EBSD characterization. The sampling location and direction are shown in Fig. 2. The rolling direction is designated as RD, the transverse direction is designated as TD, and the direction perpendicular to the RD-TD plane is referred to ND. The ND-RD (ED) plane of the sample is selected as surface for microstructure observation, which offers a suitable representation for analyzing the microstructural features. A shear deformation layer usually exists on the surface of the rolled plate, which has a significantly different microstructure from the interior. However, the overall mechanical properties

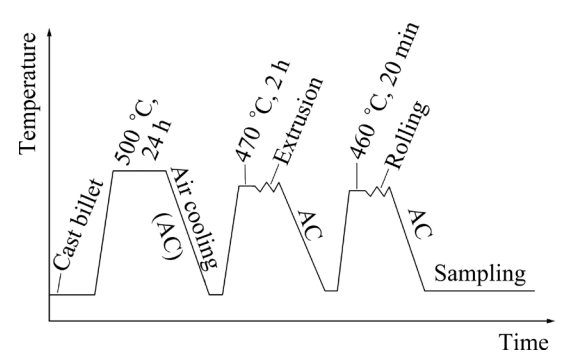


Fig. 1 Schematic diagram of extrusion and rolling processes

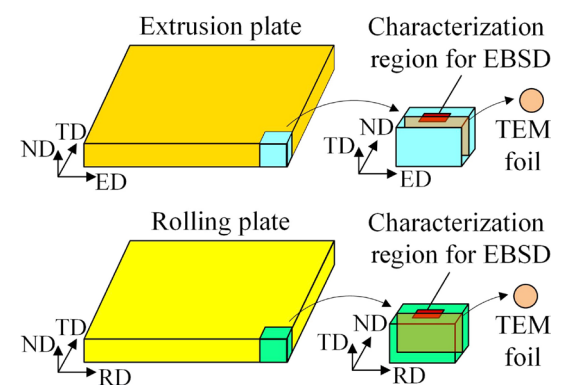


Fig. 2 Schematic diagram of sampling and characterization regions

of the plate are governed by the internal microstructure rather than by a thin surface layer. Therefore, the characterization location is chosen within the intermediate region along the ND, as shown in Fig. 2. To investigate the dislocation characteristics of different samples, transmission electron microscopy (TEM) analysis was performed. The TEM foil samples were cut from the central layer of the plate along the ND.

The EBSD samples were mechanically polished to a mirror-like finish and then electrolytically polished to remove the strain layer. The electrolyte used was a mixture of 10% perchloric acid and 90% ethanol, with electrolysis parameters of 25 V for 10 s. EBSD test was conducted on a scanning electron microscope (Zeiss Gemini 300) equipped with an EBSD attachment, and the collected data were subsequently analyzed by HKL-CHANNEL5 software. Low-angle grain boundaries (LAGBs) are defined as misorientation angle between 2° and 15°, whereas high-angle grain boundaries (HAGBs) have a misorientation angle above 15°. For quantitative analysis of the texture components, three-dimensional orientation distribution function (ODF) was computed from the

collected orientation data via a series of expansion methods. In this calculation, the maximum harmonic function $L_{\text{max}}=22$, and the Gaussian half-width required for calculating the C coefficient is set at 5°. The computed ODF was then utilized to quantitatively evaluate the volume fractions of different texture components. The pole figure was plotted using the stereographic projection method, which facilitated the analysis of the local orientation evolution. The foil samples for TEM characterization were first mechanically reduced to a thickness of 50 μm, followed by final thinning on a precision ion polishing system (Gatan PIPS II 695). The prepared foils were observed on an FEI Tecnai F20 transmission electron microscope operating at 200 kV.

3 Results and discussion

3.1 Influence of extrusion and rolling processes on grain structure

The EBSD images of the as-cast 2195 Al-Li alloy are presented in Fig. 3. The IPF map, as shown in Fig. 3(a), reveals an equiaxed grain structure in the as-cast alloy. The grain size in the alloy significantly varies, ranging from tens to

hundreds of micrometers, with an average size of $164 \, \mu m$. In Fig. 3(b), the misorientation distribution reveals that the proportion of HAGBs accounts for 88.0%, with an average misorientation angle of 39.9° . Figure 3(c) shows pole figures of the $\{110\}$ and $\{111\}$ planes, indicating a widely distributed polar density without orientation concentration. These results indicate that the grains in the as-cast alloy have random orientations.

To assess the impact of rolling deformation and temperature on the microstructure, EBSD analyses were conducted on the rolling plates with different thicknesses. Figure 4 shows IPF maps, recrystallization maps, grain boundary maps, and misorientation distributions for each sample. The black lines in the grain boundary maps represent HAGBs, whereas the red, green, and blue lines correspond to LAGBs with misorientation of $2^{\circ}-5^{\circ}$, 5°-10°, and 10°-15°, respectively. The deformed, substructured, and recrystallized grains were determined by Recrystallized Fraction Component in HKL-Channel5 software. If the average angle within a grain exceeds minimum misorientation of 2° for LAGBs, then the grain is deemed deformed and is represented in red on the map. Additionally, some grains comprise several subgrains whose internal

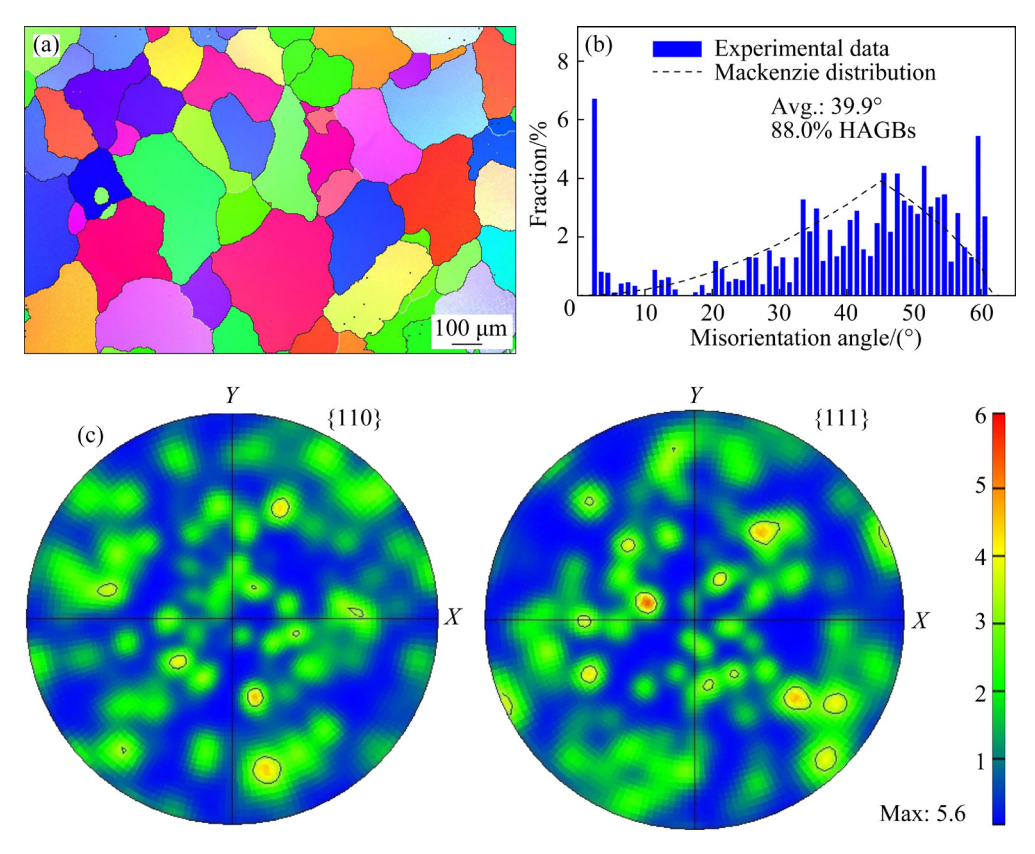


Fig. 3 EBSD images of as-cast 2195 alloy: (a) IPF map; (b) Misorientation angle distribution; (c) Pole figures

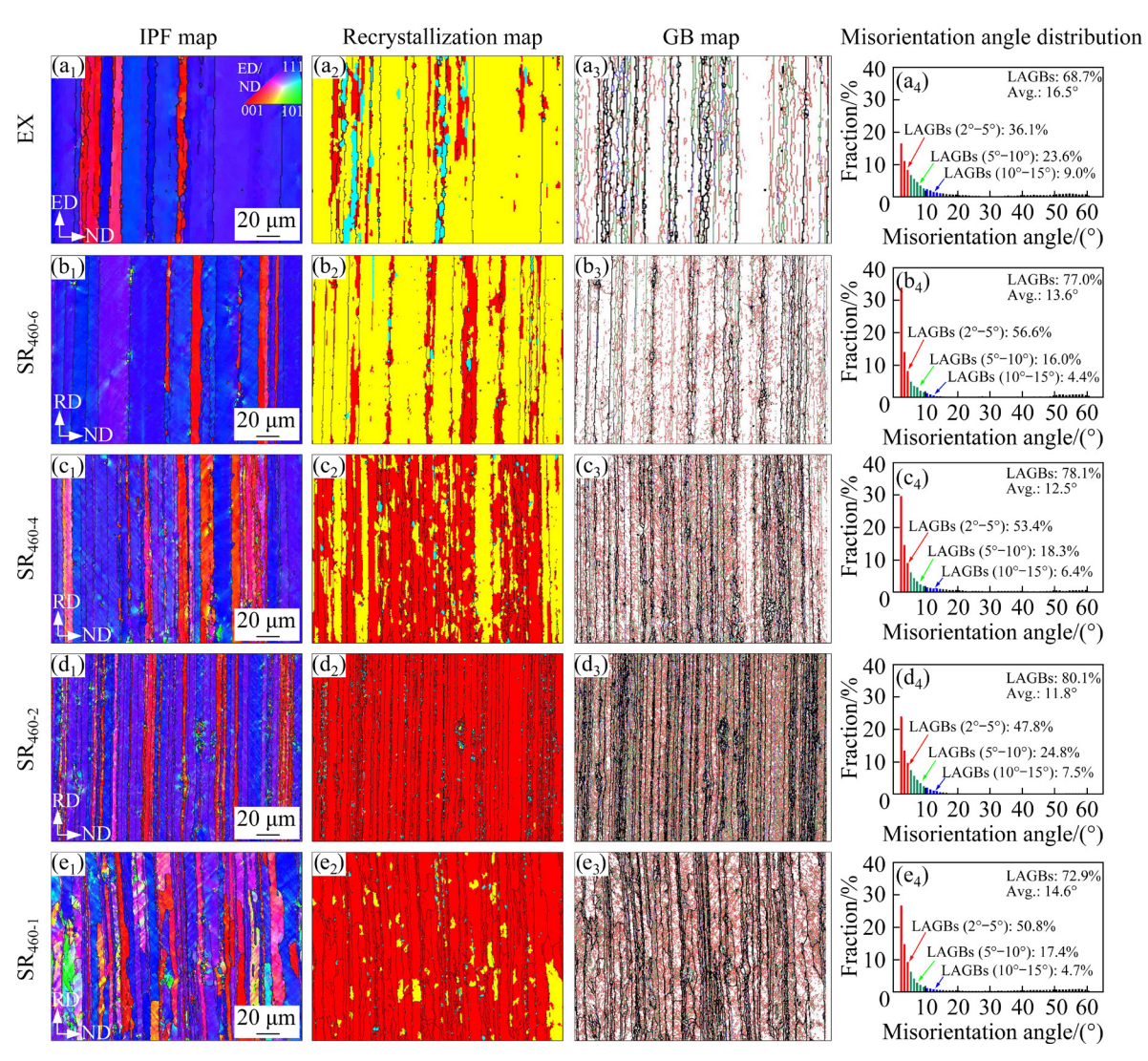


Fig. 4 EBSD images of samples produced by different processes: (a_1-a_4) EX sample; (b_1-b_4) SR₄₆₀₋₆ sample; (c_1-c_4) SR₄₆₀₋₄ sample; (d_1-d_4) SR₄₆₀₋₂ sample; (e_1-e_4) SR₄₆₀₋₁ sample

misorientation is less than 2°, but the misorientation between the subgrains exceeds 2°, which are classified as substructured grains and identified in yellow. All the remaining grains are classified as recrystallized grains marked with blue.

Figures 4(a₁—a₄) present EBSD images of the extruded sample. Elongated grains with a fibrous morphology are formed because the as-cast billet experiences substantial unidirectional stress along the extrusion direction. The grain orientations are mainly ED//(111) and (100), which are typical extrusion fiber textures. The microstructure of the plate is predominantly composed of substructure grains, with a minor presence of deformation grains and recrystallized grains. Many LAGBs exist in the grains, accounting for 68.7% of the total, with an average misorientation angle of 16.5°. During hot

extrusion processing, intense plastic deformation induces dislocation multiplication, motion, climb, and cross-slip. Simultaneously, the heat generated by intense deformation and friction elevates the temperature within the die cavity. For Al-Li alloy with high stacking fault energy (SFE), the dynamic softening mechanism at high temperatures is governed by dynamic recovery (DRV) and continuous dynamic recrystallization (CDRX) [30,31]. Dislocations undergo rapid movement and rearrangement, which results in the formation of dislocation cells and subgrain boundaries. This process contributes to the generation of a substantial quantity of LAGBs and substructured grains in the microstructure.

The EBSD results of the SR_{460-6} sample with a rolling reduction of 2 mm are shown in

Figs. $4(b_1-b_4)$. The width of the fibrous grains decreases, and the shearing bands emerge within the grains. The recrystallized grains transform into substructured grains, and more deformed grains are formed. Moreover, more LAGBs develop within the fibrous grains, and the fraction of LAGBs increases to 77.0%. Compared with that of the EX sample, the misorientation distribution of the SR₄₆₀₋₆ sample also significantly changes. There is 20.5% increase in the proportion of LAGBs with low misorientation angle of 2°-5°, leading to a relative decrease in the proportion of grain boundaries with misorientation angle above 6°. During hot rolling, dislocations are persistently generated and rapidly rearranged, resulting in the formation of new LAGBs through dynamic recovery. As a result, the newly formed LAGBs have low misorientation angle ranging from 2° to 5°.

As the rolling reduction increases, the width of grains in the SR₄₆₀₋₄ and SR₄₆₀₋₂ samples continues to decrease, and the shearing bands within the grains become increasingly dense, as shown in Figs. $4(c_1-c_4)$ and Figs. $4(d_1-d_4)$, respectively. The deformed grains emerge as the dominant grain structure, whereas the substructured grains and large recrystallized grains gradually diminish. Numerous small recrystallized grains develop within the matrix, most of which arise from the fragmentation of narrow fibrous grains. During high-temperature deformation of alloys with high SFE, deformed grains elongate and develop localized serrations under high strain. The thickness of the elongated grains decreases to less than 1-2 subgrain sizes, and the serrations along the grain boundaries pinch off, leading to the formation of fine equiaxed grains. This phenomenon, termed geometric dynamic recrystallization [17,32,33], aligns well with the microscopic features observed in the SR₄₆₀₋₄ and SR₄₆₀₋₂ samples. Additionally, the grain orientation gradually changes with the progression of rolling deformation. The grains initially oriented with \(\lambda 111 \rangle //ED\) change towards an orientation closer to (112), and the grains with (100)//ED also transform into other orientations. The special orientation evolution cannot be captured by the IPF maps and requires further analysis by means of the pole figure.

In terms of the grain boundary characteristics, the misorientation distributions indicate that the proportion of LAGBs continues to increase in both the SR₄₆₀₋₄ and SR₄₆₀₋₂ samples. However, the growth rate of LAGBs in SR₄₆₀₋₄ sample is significantly lower than that in SR₄₆₀₋₆ sample. The increase in deformation promotes the formation of new grains through the geometric dynamic recrystallization and orientation rotation at shearing bands. Additionally, the occurrence of the static recrystallization becomes more significant as the annealing between rolling passes is applied. These processes collectively result in an increase in the fraction of HAGBs, which, in turn, reduces the proportion of LAGBs and slows their growth rate. Further observation reveals differences in the misorientation angle distributions between the SR₄₆₀₋₂ and SR₄₆₀₋₄ samples. For the SR₄₆₀₋₂ sample, the proportion of grain boundaries with low 2°-5° misorientation angle of decreases significantly. Conversely, the proportion of grain boundaries with misorientations ranging 5°-15° increases greatly. This finding can be attributed to the greater rolling reduction experienced by the SR₄₆₀₋₂ sample, which results in a greater number of dislocations and greater stored energy. The alloys with high storage energy are more susceptible to both static recovery and recrystallization during interpass annealing. This facilitates a shift from low misorientation angle to medium and high misorientation angle.

A thinner plate with a thickness of 1 mm was obtained, i.e., sample SR₄₆₀₋₁, by further increasing the number of rolling passes and the reduction. Figures $4(e_1-e_4)$ show the EBSD images of the sample. The grain size of the sample significantly increases instead of the further narrowing of the fibers. Furthermore, considerable alterations in the grain orientation occur, accompanied by the presence of shearing bands within the grains. Compared with that of the SR₄₆₀₋₂ sample, the grain boundary density of the SR₄₆₀₋₁ sample is substantially reduced. Additionally, the proportion of LAGBs in the SR₄₆₀₋₁ sample decreases significantly, whereas the percentage of grain boundaries with a low misorientation angle between 2° and 5° increases. Nevertheless, no entirely recrystallized grains free of LAGBs are found. The above observations indicate that the microstructure sample undergoes significant of the SR_{460-1} recrystallization and grain coarsening, which the coarse recrystallized grains experience deformation again. Upon rolling the plate to

approximately 2 mm, as depicted in Figs. 4(d₃, d₄), a significant increase in the dislocation density and intragranular substructure is observed, leading to a substantial accumulation of storage energy. This elevated storage energy facilitates recrystallization and grain boundary migration during the interpass annealing stage prior to final deformation. Consequently, coarse recrystallized grains are formed. These grains are further deformed in the final rolling pass, generating new LAGBs primarily exhibiting a misorientation angle ranging 2°–5°.

According to the above analysis, the critical strain inducing significant recrystallization and rapid grain coarsening during rolling deformation of the extrusion plate is between 1.4 and 1.9 (rolling reduction of approximately 75%–85%). Once the

strain exceeds this critical value, rapid recrystallization and grain coarsening occur in a short period.

To examine the microstructure evolution of the 2195 alloy under intense shear deformation, asymmetric rolling experiments were performed at various differential speed ratios. Figure 5 shows the EBSD images of the rolled plates. Figure 5(a) clearly shows that the grain structure resulting from asymmetric rolling significantly differs from that obtained through synchronous rolling. Coarse grain layers approximately 100–200 µm thick are formed on the plate surfaces. Within the plate, a layered microstructure is observed with alternating coarse and fine grains. The grain orientations are completely randomized. The misorientation distribution presented in Fig. 5(b) reveals that the

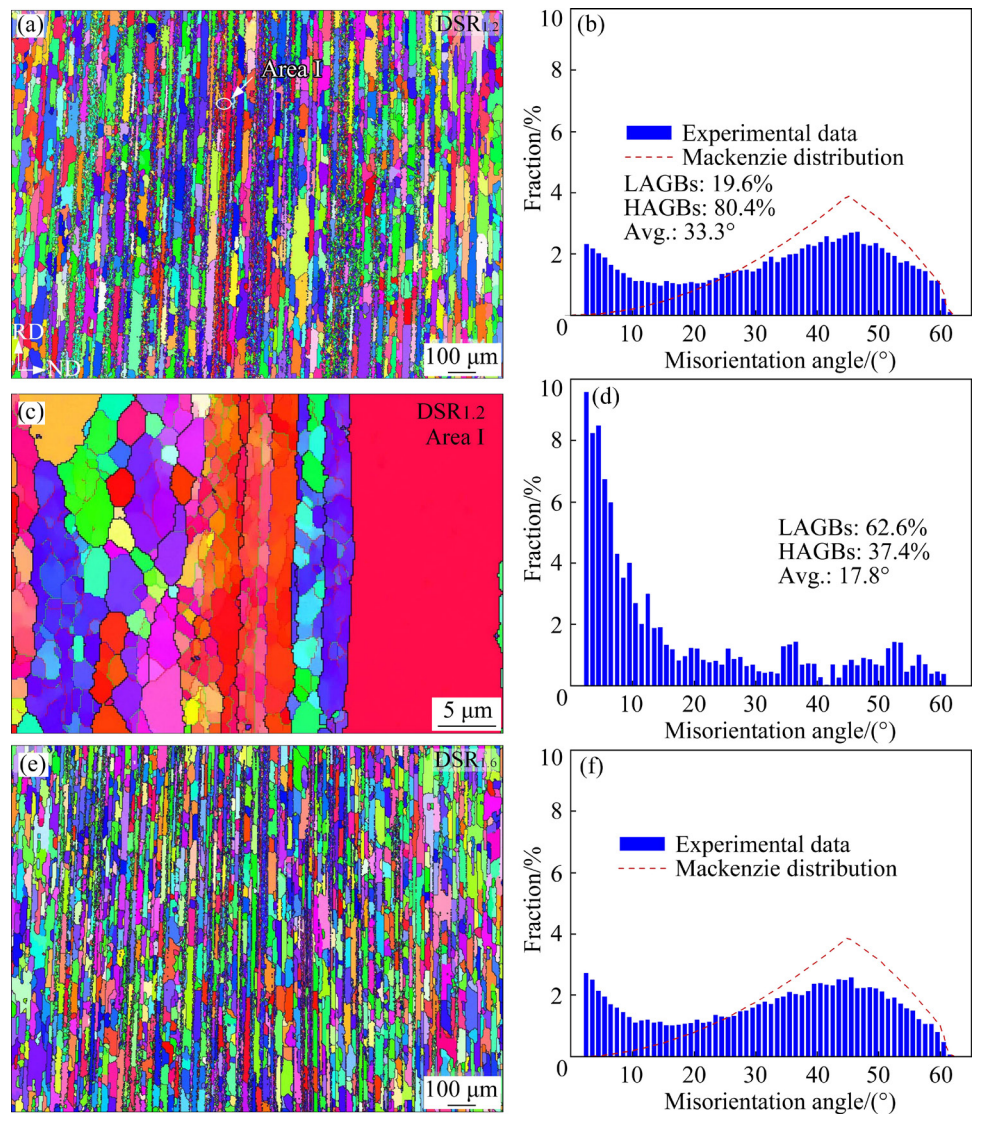


Fig. 5 EBSD images (a, c, e) and statistics of grain boundary distributions (b, d, f) of asymmetrically rolled samples: (a, b) DSR_{1,2} sample; (c, d) Area I in (a); (e, f) DSR_{1,6} sample

proportion of HAGBs amounts for 80.4% and aligns well with the Mackenzie distribution curve, indicating that the grains adopt a predominantly random orientation [34]. These findings suggest that the plate experiences thorough recrystallization process during asymmetric rolling.

Figure 5(c) presents an enlargement of Area I to provide a clearer morphology of the fine-grained region. The grain size within the fine-grained region mostly ranges from 5 to 10 µm. These fine grains result from fragments of the original fibrous grains. Notably, the boundaries of small grains are delimited partly by LAGBs and partly by HAGBs. These characteristics are typical results of the continuous dynamic recrystallization processes [35–37]. During asymmetric rolling, the plate experiences severe shear deformation, leading to higher strain than that during synchronous rolling. A greater stored energy provides a strong driving force for recrystallization. Furthermore, shear strain facilitates grain rotation and the formation of distinct orientations [38,39]. A more random orientation tends to cause grain coarsening during interpass annealing.

Figures 5(e, f) present the IPF maps and misorientation distributions of the rolled plate with a differential ratio of 1:1.6. The grain morphology and orientation under the high differential ratio are consistent with those observed in DSR_{1.2} sample. Therefore, under high-temperature deformation conditions, shear deformation is more prone to induce recrystallization and grain coarsening. However, once the critical conditions are met, further increasing the shear degree has little effect on the microstructure.

Figure 6 presents TEM images of samples under different deformation conditions, revealing the changes in dislocations within the grains. The overall morphology of the dislocations was observed at a lower magnification, and then the dislocation density and distribution for different samples were compared under the same zone axis of $\langle 011 \rangle_{Al}$. In the hot extruded plate (EX sample), the dislocation density is low and exhibits a relatively uniform and dispersed distribution, as shown in Figs. 6(a, b). After rolling with a reduction of 2 mm (SR₄₆₀₋₆ sample), an increase in the number of dislocations is observed, with localized accumulation as indicated by the yellow boxes in Fig. 6(d). As the rolling reduction

increases to 4 mm (SR₄₆₀₋₂ sample), the dislocation within the matrix becomes exceedingly dense, as depicted in Figs. 6(e, f). Even at high magnification, the dispersed dislocation lines become difficult to discern. Therefore, the accumulated dislocation density in the alloy gradually increases as deformation intensifies, which is consistent with the results from the EBSD analysis presented in Fig. 4.

Figures 6(g, h) present TEM images of the asymmetrically rolled sample DSR_{1,2}. A certain number of dislocations can be observed in large grains, but the dislocation density is much lower than that of the synchronous rolling sample SR₄₆₀₋₂. In addition, numerous small microscale grains are visible in the DSR_{1.2} sample. These small grains exhibit an absence of dislocations, which are probably formed by recrystallization as new grains. The microstructure is consistent with the mixed grain structure previously shown in Fig. 5(a). This phenomenon confirms the occurrence of dynamic recrystallization in DSR_{1.2} sample. The dislocations present in large grains are produced by further deformation of the growing recrystallized grains. These findings of dislocation evolution further confirm that under identical deformation temperature and reduction, asymmetric rolling has a greater propensity for inducing dynamic recrystallization than synchronous rolling does.

3.2 Influence of extrusion and rolling processes on texture

To further analyze the texture types and variations in the samples subjected to different processes, Fig. 7 shows ODF sections at φ_2 values of 15°, 20°, 45°, 75°, and 80°. The color lines in the sections outline the positions of the four primary deformation textures: Cu $\{112\}\langle 11\overline{1}\rangle$, Ex $\{123\}\langle 11\overline{1}\rangle$, S $\{123\}\langle 63\overline{4}\rangle$, and Bs $\{011\}\langle 21\overline{1}\rangle$. The maximum deviation angle from the ideal positions of the textures is 15°.

As can be seen, four kinds of deformation textures are included in the extrusion and rolling plates. However, the intensity of the texture components varies in the samples according to the processing conditions. The Ex and Cu components exhibit the highest intensity in the extrusion plate, whereas the Bs and S components are slightly weaker, with a trace amount of Cube component. As the degree of rolling deformation increases, the intensities of the Ex and Cu components in the

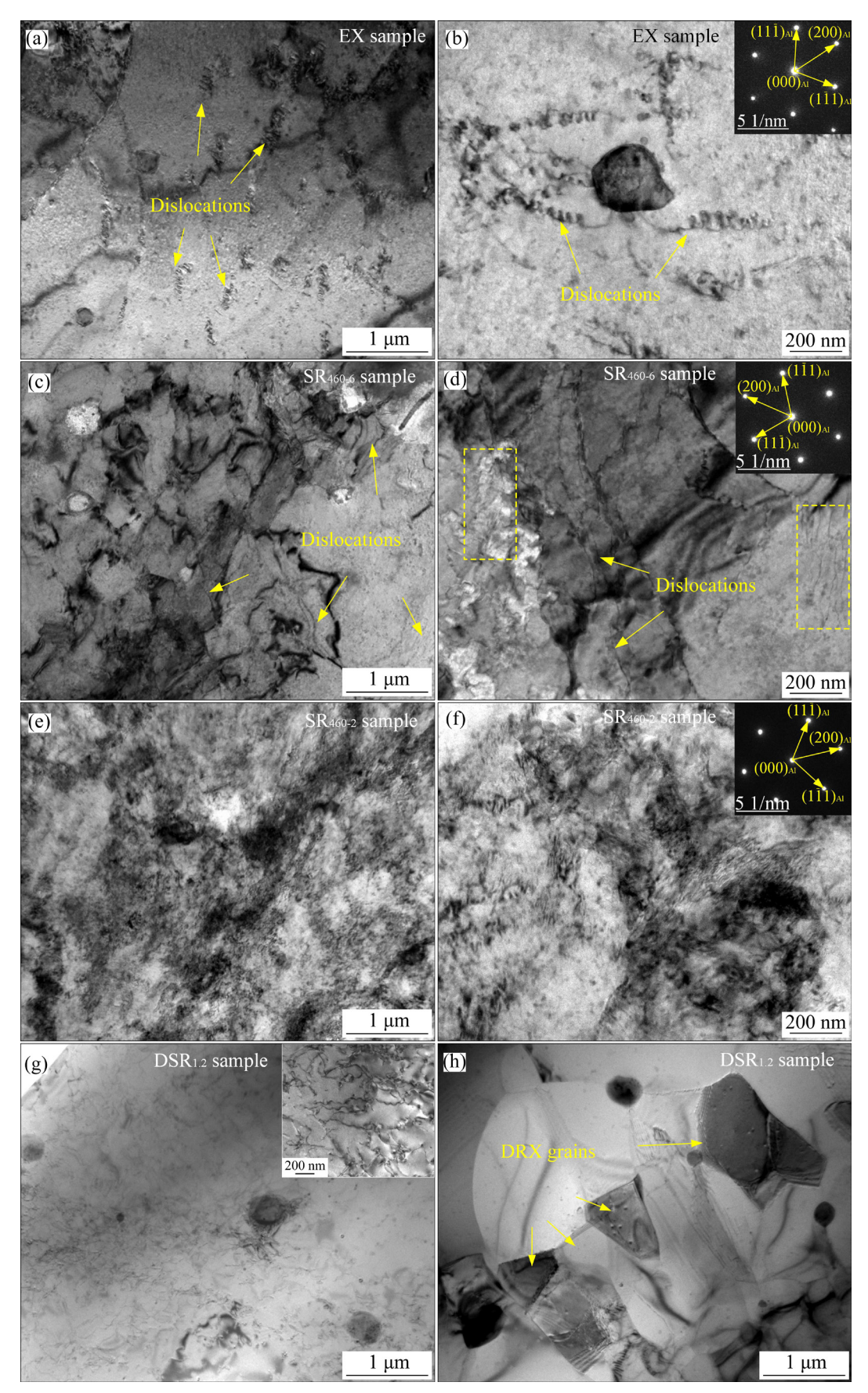


Fig. 6 TEM images of samples under different deformation conditions: (a, b) EX sample; (c, d) SR_{460-6} sample; (e, f) SR_{460-2} sample; (g, h) $DSR_{1.2}$ sample (Inset shows dislocations at high magnification)

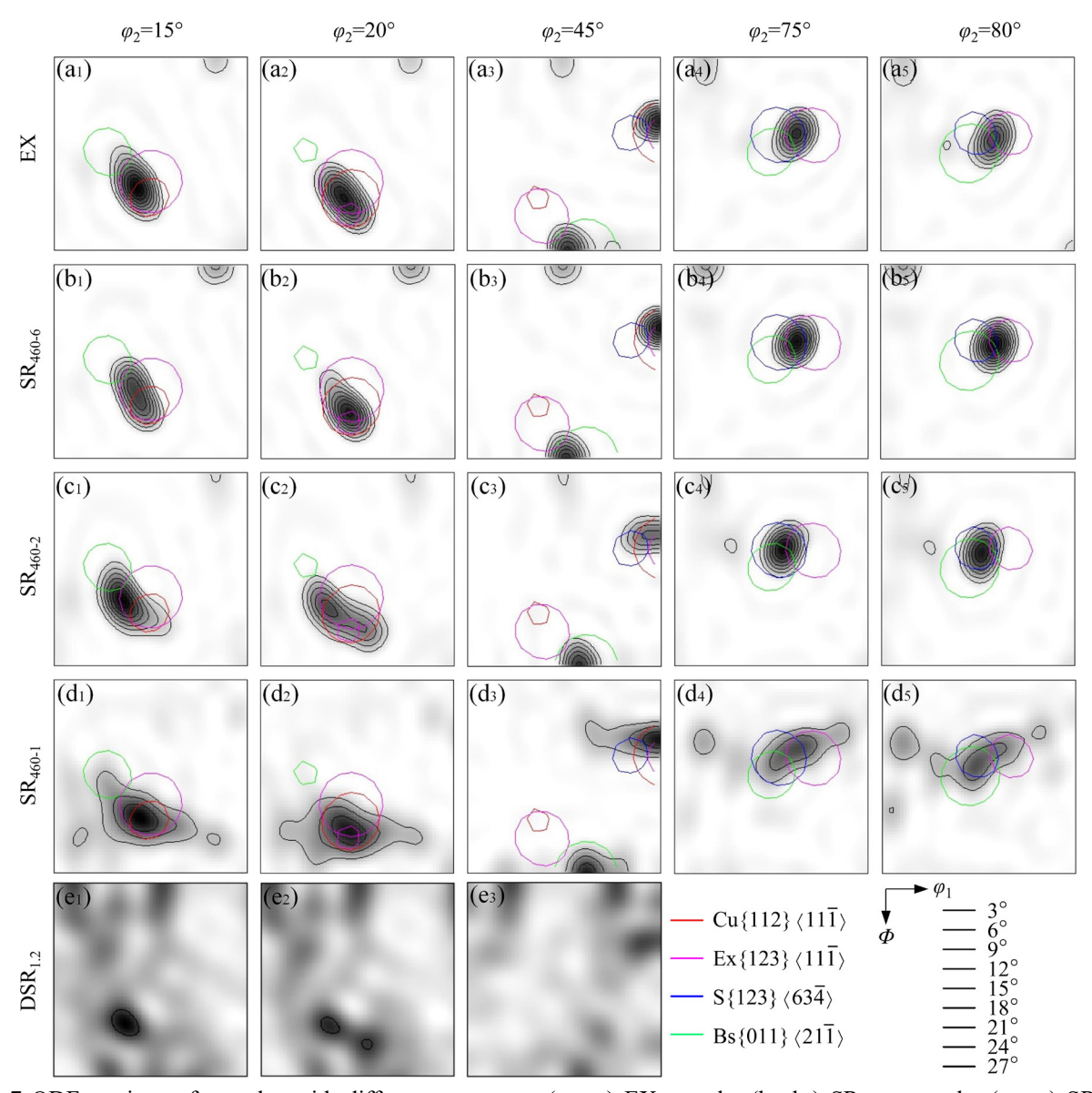


Fig. 7 ODF sections of samples with different processes: (a_1-a_5) EX sample; (b_1-b_5) SR₄₆₀₋₆ sample; (c_1-c_5) SR₄₆₀₋₂ sample; (d_1-d_5) SR₄₆₀₋₁ sample; (e_1-e_3) DSR_{1.2} sample

SR₄₆₀₋₆ and SR₄₆₀₋₂ samples decrease and deviate progressively from their ideal positions. In contrast, the S component intensity increases significantly and shifts towards its ideal position. As the rolling deformation further increases, all textures within the SR₄₆₀₋₁ sample obviously weaken, because strong dynamic recrystallization occurs above the critical deformation degree and gives rise to new grains with random orientations. Moreover, the asymmetrically rolled sample, DSR_{1.2}, exhibits a more random orientation, as confirmed by the ODF sections presented in Figs. 7(e₁–e₃), which agrees with the observations in Fig. 5.

Table 2 lists the proportions of primary texture components present in each sample. The proportion

of the \(\frac{111} \)/ED fiber texture is approximately 50% in the extrusion plate, with the Ex component attaining the highest proportion at 31.5% and the Cu component accounting for 18.3%. As the rolling process progresses, the texture components change in two trends. On the one hand, the proportions of Ex and Cu components decrease gradually, which is more obvious at larger deformations. On the other hand, the proportion of the S component has a large increase. The proportions of Ex and Cu components decrease to 11.5% and 7.3%, respectively, in the SR₄₆₀₋₂ sample, whereas the S proportion increases to 31.9%. Additionally, the Bs component remains relatively stable, and the Cube component always maintains at a low level of intensity. These changes

| Texture type | Euler angle/(°) | | | Texture component fraction/% | | | | | |
|-------------------------------------------|-----------------|----|-------------|------------------------------|---------------------|---------------------|---------------------|---------------------|----------------|
| | φ_1 | Φ | φ_2 | EX | SR ₄₆₀₋₆ | SR ₄₆₀₋₄ | SR ₄₆₀₋₂ | SR ₄₆₀₋₁ | $DSR_{1.2} \\$ |
| Ex $\{123\}\langle 11\overline{1}\rangle$ | 43 | 58 | 18 | 31.5 | 28.1 | 13.3 | 11.5 | 11.8 | 2.2 |
| Cu $\{112\}\langle 11\overline{1}\rangle$ | 90 | 35 | 45 | 18.3 | 12.0 | 10.0 | 7.3 | 6.0 | 1.9 |
| $S\{123\}\langle 63\overline{4}\rangle$ | 59 | 37 | 63 | 14.6 | 15.3 | 20.3 | 31.9 | 10.4 | 6.4 |
| Bs $\{011\}\langle 21\overline{1}\rangle$ | 35 | 45 | 0 | 13.2 | 16.1 | 13.1 | 16.0 | 10.0 | 2.9 |
| Cube {001} \langle 100 \rangle | 0 | 0 | 0 | 2.8 | 4.2 | 2.2 | 2.2 | 0.7 | 0.8 |

Table 2 Proportion of each texture component in samples with different processes (Deviation angle of 10°)

in texture proportion result in a shift of the $\langle 111 \rangle$ //RD fiber texture towards a nearly $\langle 112 \rangle$ //RD orientation. Upon exceeding the critical rolling deformation, strong recrystallization and grain coarsening occur within the microstructure, leading to a notable reduction in texture intensity. Therefore, the SR₄₆₀₋₁ sample has smaller proportions of each texture. The texture weakening due to recrystallization is more prominent in the asymmetric rolling sample, DSR_{1.2}.

The components included in the β -fiber texture have distinct characteristics. Compared with the Bsoriented grains, grains with S and Cu orientations contain more intragranular substructures and store more energy [40,41]. With increasing deformation, there is a clear increase in the dislocation density and number of LAGBs within the grains, which facilitates the formation of a high-storage-energy S texture. Additionally, the S-oriented grains with higher storage energy are more susceptible to recrystallization, whereas the Bs-oriented grains exhibit greater resistance to recrystallization. Therefore, in the SR₄₆₀₋₁ sample experiencing significant recrystallization precess, the intensity of the S component decreases greatly, whereas the Bs component remains relatively stable.

3.3 Micro-mechanism of texture evolution

The extrusion plate mainly includes four deformation textures, namely, Ex, Cu, S, and Bs, with a minor presence of $\langle 100 \rangle$ //ED fiber texture. The evolution of the grain orientation is closely associated with the strain. Therefore, it is necessary to pinpoint the strain behavior during the rolling process. Commonly, the rolled plate significantly extends along the RD (x) and becomes thin in the ND (z), with minimal deformation in the TD (y). Therefore, the slip systems in the deformed grains primarily lead to displacements in the RD and ND,

causing the grains to rotate around the TD and ND axes to release ε_{xz} and ε_{xy} strains [42].

On the basis of the analysis of the IPF maps in Section 3.1, the evolution of the crystallographic texture in the rolling plate can be attributed to both the overall change in grain orientation and the local orientation transformation at the shearing bands. Therefore, in the subsequent analysis, pole figures are utilized to assess the evolution behavior comprehensively by considering both the overall and local orientation alterations.

3.3.1 Transformation among Cu, Ex, and S components

Figure 8 shows the IPF maps of the EX, SR₄₆₀₋₆, and SR₄₆₀₋₄ samples. The distribution maps for various texture components in each sample are also presented. The proportions of Ex and Cu components decrease as the degree of rolling deformation increases, and the proportion of Ex component decreases more significantly. Conversely, the content of S texture component greatly increases, which is in agreement with the results presented in Table 2. Furthermore, the colors corresponding to the Ex and Cu components appear to gradually fade, whereas the color for the S component tends to deepen. This suggests that the Ex and Cu components deviate from their ideal orientations as the degree of rolling deformation increases, whereas the S component aligns closer to its ideal orientation.

The distribution maps of the Ex, Cu, and S components are superimposed in Figs. $8(a_1-c_1)$. There is minimal overlap between the positions of the Ex and S components in the EX sample, whereas a noticeable overlap exists between the Ex and Cu components. The triaxial compressive stress in the process of extrusion leads to a preferential orientation of $\langle 111 \rangle$ //ED. However, the constraints imposed on the TD and ND are relatively weak,

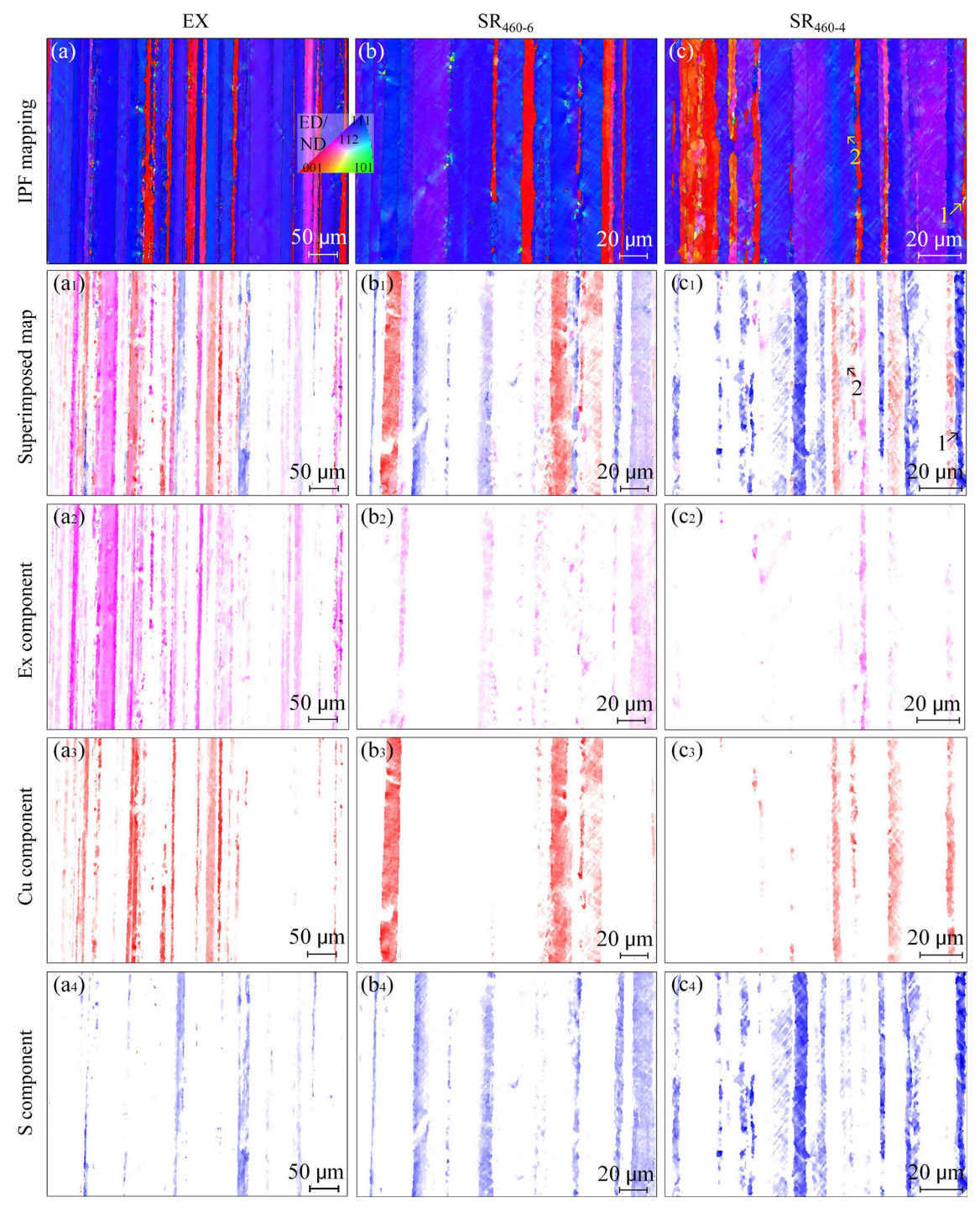


Fig. 8 IPF maps and texture component distribution maps of samples with different processes: (a, a_1 – a_4) EX sample; (b, b_1 – b_4) SR₄₆₀₋₆ sample; (c, c_1 – c_4) SR₄₆₀₋₄ sample

which results in a significant dispersion of orientation in these two directions. Therefore, the Ex and Cu components mutually include each other. Additionally, the proportion of the S component in the EX sample is relatively small, thus reducing the likelihood of overlap with other components. As rolling progresses, the S component in the SR₄₆₀₋₆ sample increases greatly, resulting in substantial

overlap with the Ex component. Notably, with the further increase of rolling deformation, the degree of overlap between the Ex and S components in the SR₄₆₀₋₄ sample turns to decrease, and most areas in the map are occupied by a single S component. These findings indicate that Ex-oriented grains in the extrusion plate gradually transform into S-oriented grains during rolling deformation,

leading to a significant increase in the content of S texture. The superimposed maps also demonstrate that the Cu component has minimal overlap with the S component in each sample, which implies that Cu-oriented grains rarely directly transform to the S orientation. However, there is a certain degree of overlap between the Cu and Ex components, which suggests a potential transformation relationship between these two texture components.

To reveal the evolution traces among the Ex, Cu, and S components, pole figure analyses are carried out on the specific local positions in the IPF Map. First, a transition region from the Ex to S orientation is identified in Fig. 8(c) and marked with Arrow 1. Then, pole figures of three points along the arrow direction are plotted in Fig. 9. It can be found that the orientation of Ex (213)[11 1]

transforms to $S(213)[\overline{364}]$ by a 16.1° rotation around the ND axis. In the process of rolling, the plate exhibits dominant elongation in the RD, which leads to a maximum shear strain of ε_{xy} . The grains tend to rotate around the ND axis under these strain conditions, facilitating a transition from the Ex to S orientation. This orientation evolution results in a significant increase in the S texture component and a notable decrease in the content of Ex component.

Figure 10(a) shows a schematic diagram of the orientation transition from ideal Cu to S. Cu-oriented grains require rotations of 10.9° around the RD axis and 16.1° around the ND axis to achieve the ideal S orientation. However, minimal deformation occurs in the TD during the rolling process, resulting in a low shear strain of ε_{yz} . This

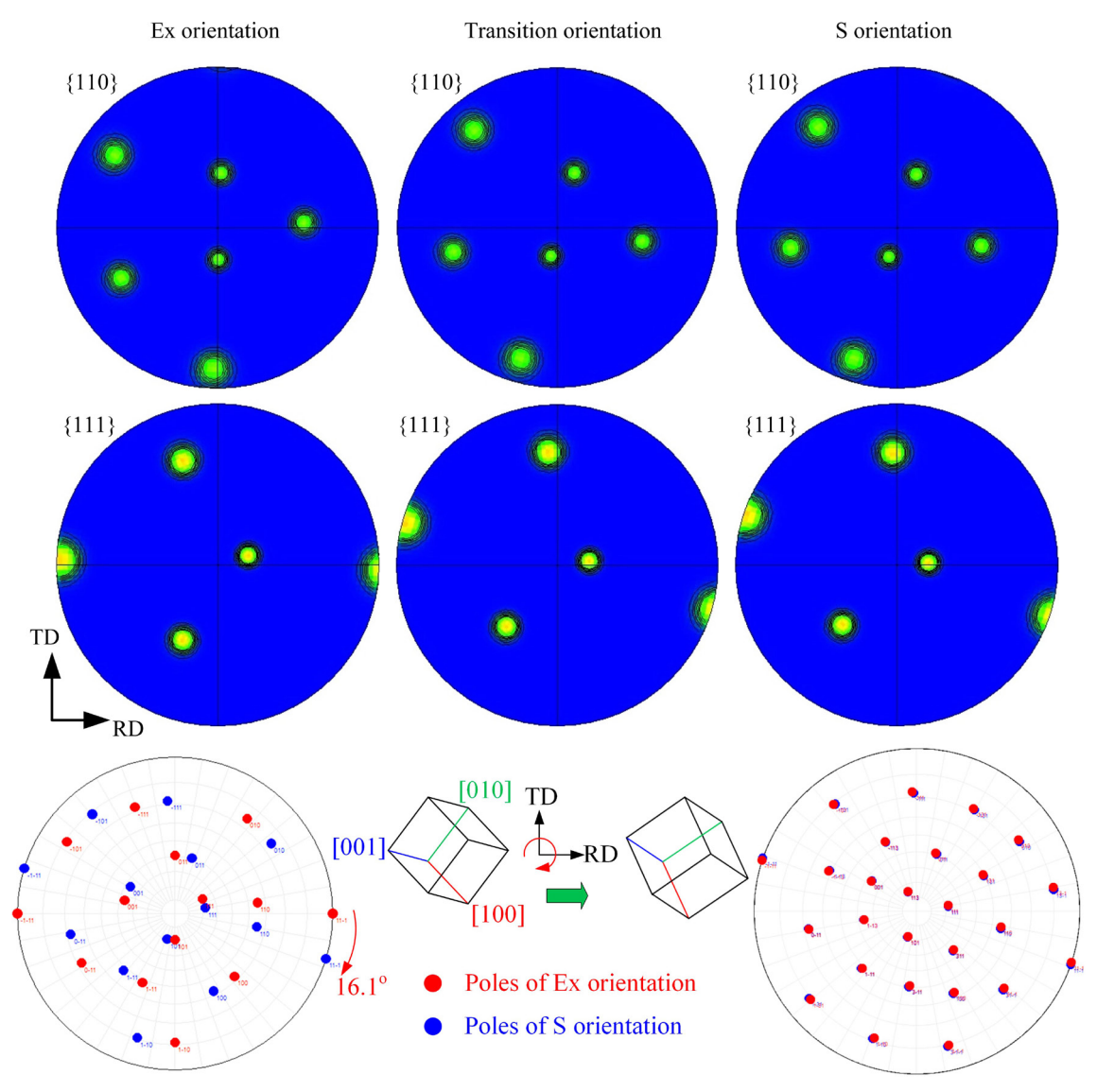


Fig. 9 Pole figures of three points on path shown by Arrow 1 in Fig. 8(c) and schematic diagram of transition from Ex to S orientation

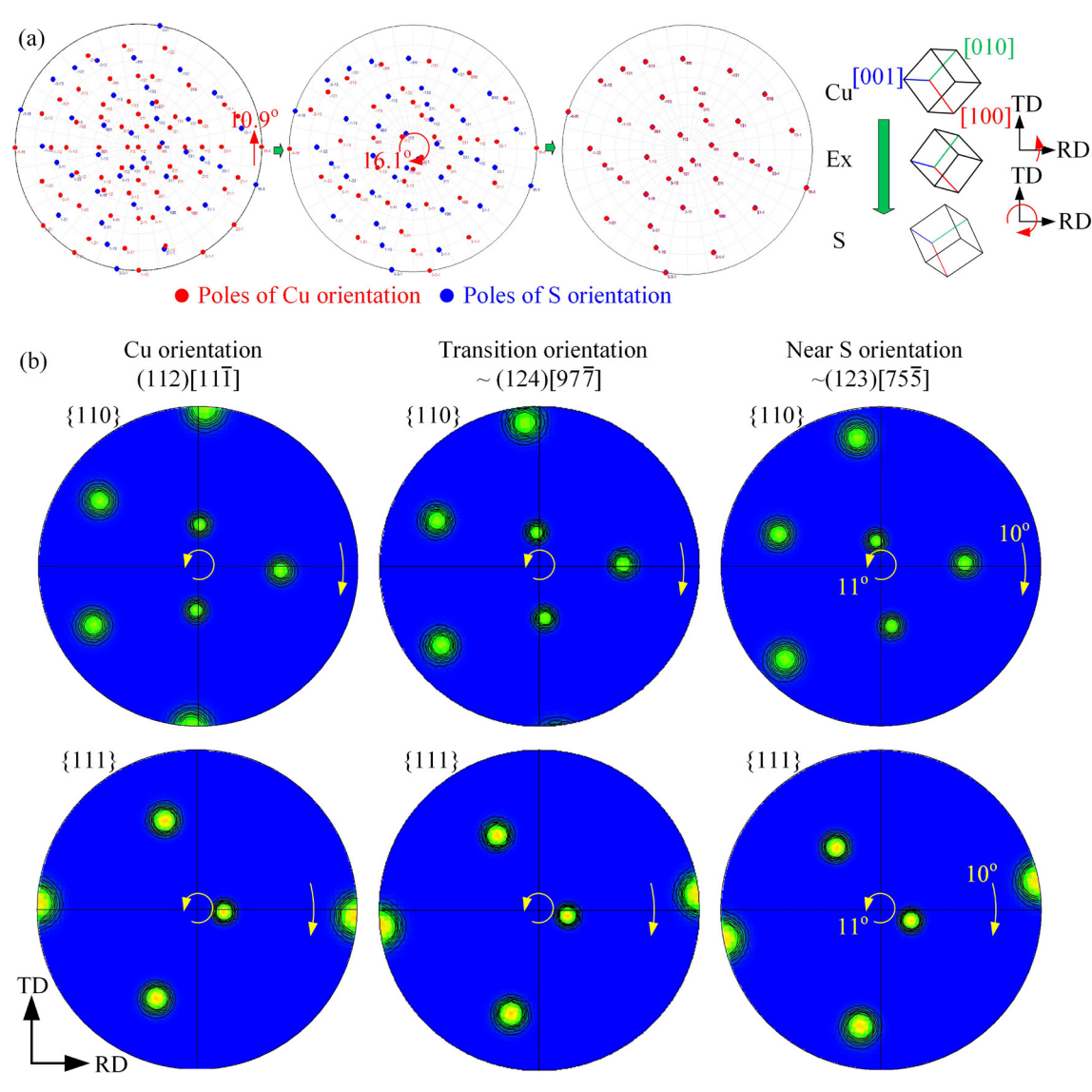


Fig. 10 Schematic diagram of transition from ideal Cu to S orientation (a) and evolution of pole figure (b) on path shown by Arrow 2 in Fig. 8(c)

constraint limits the grain rotation around the RD axis, thus impeding the transformation from the Cu orientation to the Ex or S orientation. Similarly, rotational hindrance in the RD also restricts the transition of Ex towards the Cu orientation. Consequently, under small degree of rolling deformation, the mutual transformation between Ex and Cu is less noticeable in Fig. 8.

As the degree of rolling deformation increases, however, the change in orientation becomes more complex because the grains in the polycrystalline alloy interfere with and constrain each other for coordinated deformation [43,44]. Therefore, unexpected evolution paths appear in samples with large deformations. Figure 10(b) shows the pole figures of three positions on the path shown by

Arrow 2 in Fig. 8(c). The Cu orientation rotates around the ND and RD axes, leading to shifts in both the crystallographic plane and orientation. The Miller indices gradually change from (112)-[111] to (123)[755] via (124)[977], forming an orientation between Ex and S. This type of orientation deviates from the Cu component and can be identified as any one of the Cu, Ex, or S components.

3.3.2 Evolution of Bs and S texture components

In addition to the Ex, Cu, and S components, $Bs\{011\}\langle 21\overline{1}\rangle$ is also found in the extrusion plate. The evolution of the Bs texture during the rolling exhibits distinct characteristics. LI et al [6] proposed that dislocation slip takes place on two equivalent slip planes when grains with the Bs

orientation experience deformation. This slip symmetry endows the orientation stability of the Bs component. However, this stability decreases as the rolling deformation increases to high levels, which causes the Bs orientation to change along unexpected paths.

Figure 11(a) shows an IPF map of the SR₄₆₀₋₂ sample at high magnification, in which the grains with near Bs and R-Bs orientations are highlighted. The orientations in many local areas within Grain A deviate from Bs because of the high degree of rolling deformation. A local area is selected and marked by Arrow 1, where the ideal Bs orientation transforms to another. The pole figures are then

plotted on three points along the path indicated by Arrow 1. The Bs (011)[211] orientation undergoes an 18° rotation around the RD axis and transforms into the (153)[211] orientation. This orientation is very close to S (132)[643], with a deviation of only 3.5° around the TD axis. Therefore, it is reasonable to conclude that Bs-oriented grains gradually approach the S orientation during the rolling deformation. HIRSCH and LÜCKE [42] reported that changes in the grain shape during the rolling process can lead to a decrease in the Bs orientation stability and result in a transition to S orientation. CHOWDHURY [45] also observed that the Bs orientation evolves into the S orientation during the

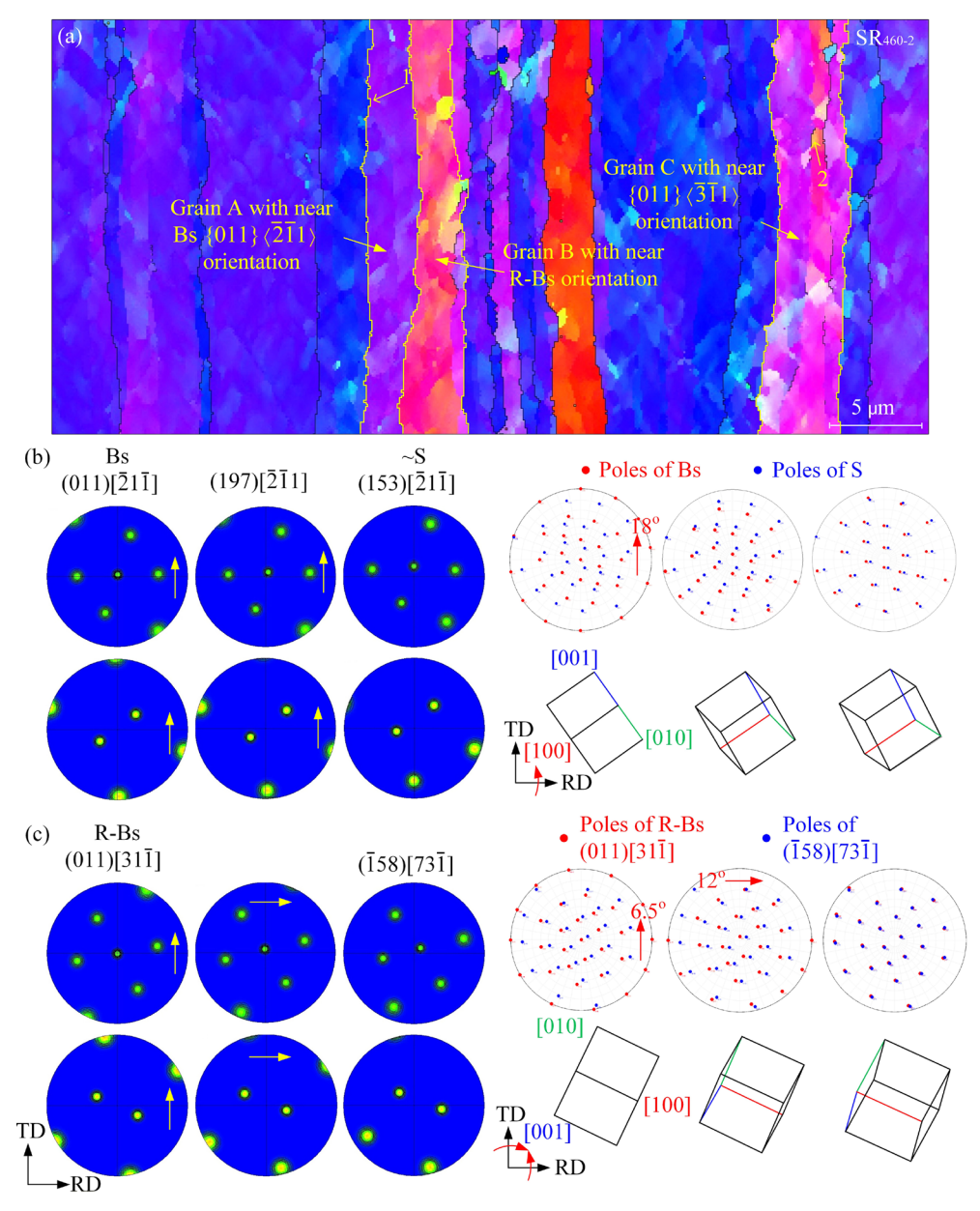


Fig. 11 IPF map of SR_{460-2} sample (a); Pole figures and corresponding evolution schematic diagrams along path shown by Arrow 1 (b) and Arrow 2 (c) in (a)

rolling process in a 5182 aluminum alloy. Figure 8 clearly illustrates that the fibrous grains exhibit a significant reduction in thickness when subjected to extensive rolling deformation, which results in a flattened morphology. This deformation induces an ε_{yz} strain and triggers a rotation in the grain orientation around the RD axis. This finding also offers an explanation for the phenomenon that the Cu orientation gradually approaches to the S/Ex orientation during large deformation.

The extrusion plate contains a small number of variants of the Bs component, which mainly consists of R-Bs formed by the rotation of Bs around the ND axis. The most representative example is the component with a Miller index of $\left\{011\right\}\left\langle31\,\overline{1}\right\rangle$, which arises from a 10° rotation of Bs around the ND axis. The path indicated by Arrow 2 in Fig. 11(a) is a typical evolution of the R-Bs $\left\{011\right\}\left\langle31\,\overline{1}\right\rangle$ orientation. Figure 11(c) presents pole

figures of three points along this path. The R-Bs $(011)[31\overline{1}]$ orientation rotates around both the RD and TD axes and gradually evolves into the $(\overline{1}58)[73\overline{1}]$ orientation, which is distinct from the evolution of the Bs orientation.

More generally, a series of R-Bs components with different orientation indices can be generated by rotation of Bs around the ND axis with various angles. To further investigate the evolution of the R-Bs type orientations, Grain B is highlighted in Fig. 11(a), in which a series of orientations near R-Bs are included. The pole distribution map projected by Grain B is presented in Fig. 12(a). Clearly, there are two types of orientations within the grain. The red poles primarily result from a 20° rotation of the R-Bs (011)[522] orientation around the RD axis, whereas the purple poles result from a 15° rotation of the R-Bs (011)[411] orientation around the RD axis. Moreover, these two types of

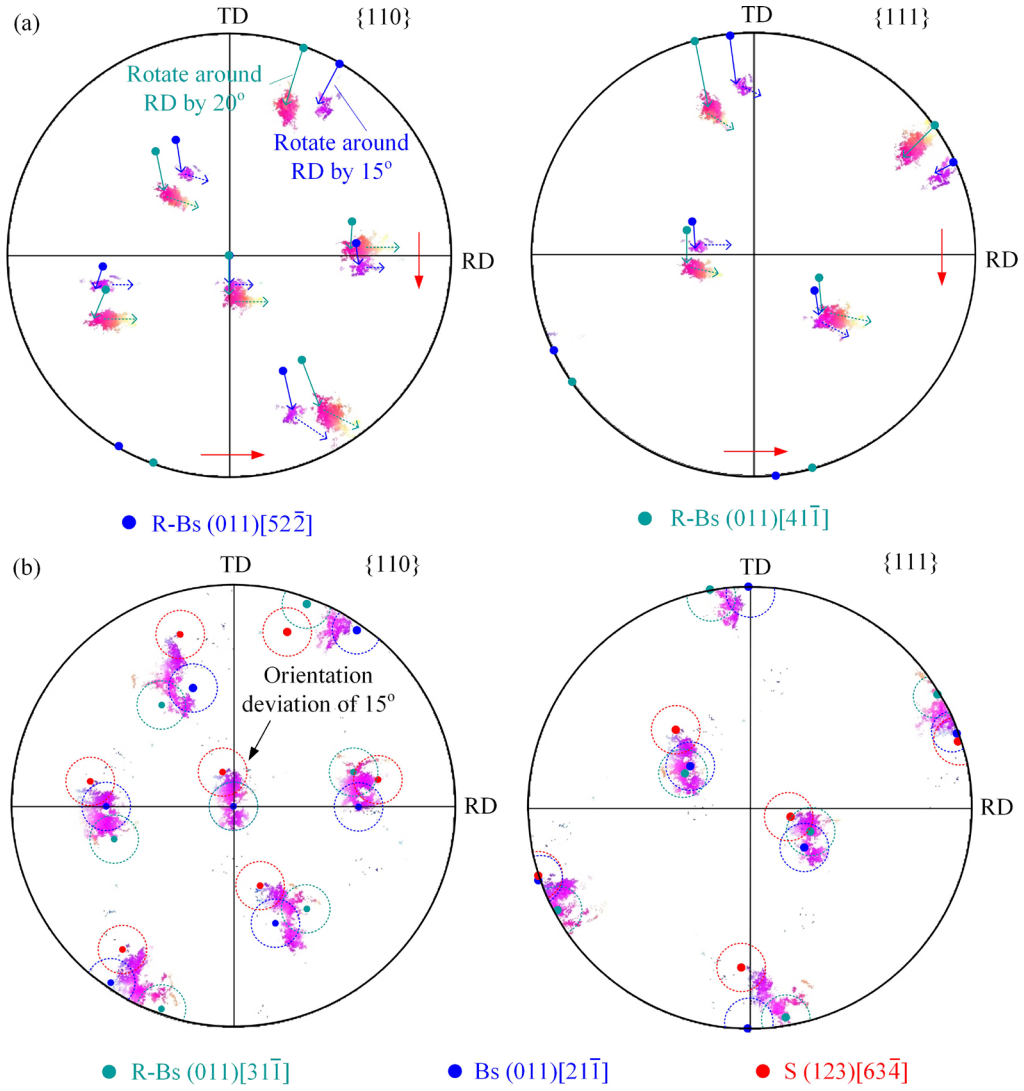


Fig. 12 Pole distribution maps of Grain B (a) and Grain C (b) in Fig. 11(a)

poles tend to rotate around the TD axis and transform to other orientations. On the basis of the analysis, it can be concluded that the R-Bs type orientations have similar evolution mode, both of which rotate around the RD and TD axes and evolve towards other orientations. In contrast to Bs, the R-Bs type orientations do not transform to the S orientation. Moreover, the greater the deviation from the initial orientation of the Bs is, the more divergent the final orientation is from S.

Alternatively, the evolution of R-Bs type orientations can be analyzed from another perspective. During the rolling process, Bs-oriented grains rotate around the ND, RD, and TD axes by variable angles owing to differences in the grain shape, strain state, and orientation deviation. As a result, a series of R-Bs type orientations are formed. As the rolling deformation increases, the orientation deviation becomes increasingly amplified and leads to the formation of new grains with the distinct orientations. This phenomenon manifests as grain fragmentation or geometric dynamic recrystallization in the IPF map. In this sense, the evolution components from R-Bs can encompass three textures: Bs, R-Bs, and S. Therefore, the orientation evolution behavior described can also be applicable to the three components. Figure 12(b) presents the pole distribution of Grain C in Fig. 11(a), which has a near R-Bs(011)[31 1] orientation. The circles in this figure represent the corresponding texture ranges with a deviation angle of 15°. It is evident that R-Bs (011)[31 1], Bs, and S cannot individually cover all poles from the grain. In addition, a few poles lie outside the ranges of all three textures. This suggests that, approximately the same initial orientations (such as Bs, R-Bs, and S in the nonideal position) undergo increasing deviation as deformation progresses and move towards different final destinations. This process ultimately leads to the formation of new fragmented grains with distinct orientations.

3.3.3 Evolution of Cube texture component

The extrusion plate contains a minor quantity of Cube $\{001\}\langle100\rangle$ texture components, which primarily exist in the form of $\langle100\rangle$ //ED fiber texture. As rolling progresses, the Cube orientation undergoes evolution. Figure 13(a) shows IPF map of the SR₄₆₀₋₂ sample, in which a local region within the Cube-oriented grain is selected to analyze the orientation evolution. The pole figures of three points along the arrow are plotted in Fig. 12(b). The ideal Cube (001)[010] orientation rotates around

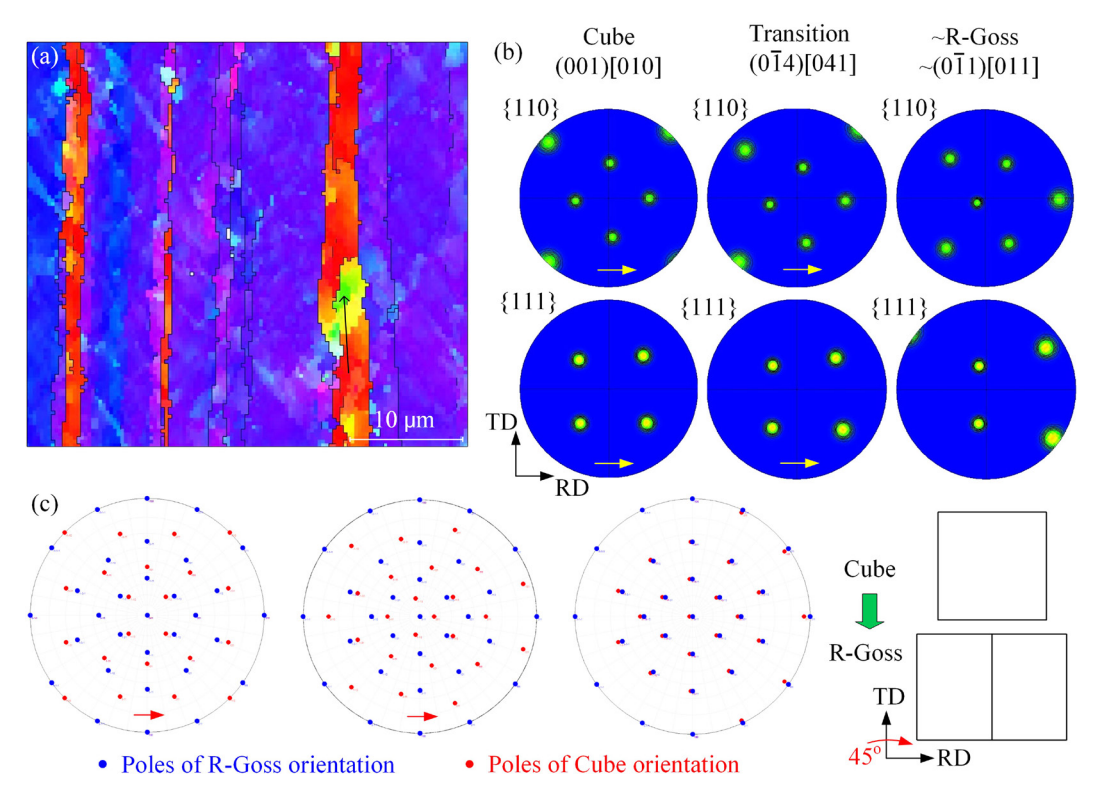


Fig. 13 IPF map of SR₄₆₀₋₂ sample (a); Pole figures along path marked by arrow (b) in (a); Schematic diagram of evolution from ideal Cube towards R-Goss orientation (c)

the TD axis and gradually aligns with the R-Goss $(0\overline{1}1)[011]$ orientation via the orientation of $(0\overline{1}4)[041]$. For clarity, a schematic diagram depicting the pole movement and lattice rotation is provided in Fig. 12(c). The red Cube poles require a 45° rotation around the TD axis to align with blue R-Goss poles. Notably, Figs. 8(c) and 13(a) reveal that the initial Cube component rarely transforms entirely into R-Goss during the rolling process. Instead, it tends to stabilize at an intermediate orientation along this transformation pathway.

3.3.4 Local orientation evolution of shearing bands

In addition to the general orientation transformation, shearing bands within the grains

also induce local orientation changes. As the degree of rolling deformation increases, the shearing bands become denser, and the local orientation transformation becomes more pronounced, which significantly influences the texture evolution of the rolling plate. To gain insights into the evolution at the shearing bands, the orientations of the shearing bands in the grains with four main orientations of Cu, Ex, S, and Bs are examined via pole figures. Figures 14(a, b) show the IPF maps for the SR₄₆₀₋₄ and SR₄₆₀₋₂ samples, in which the points for local orientation analysis are marked. The corresponding pole figures at each point are presented in Figs. 14(c-f).

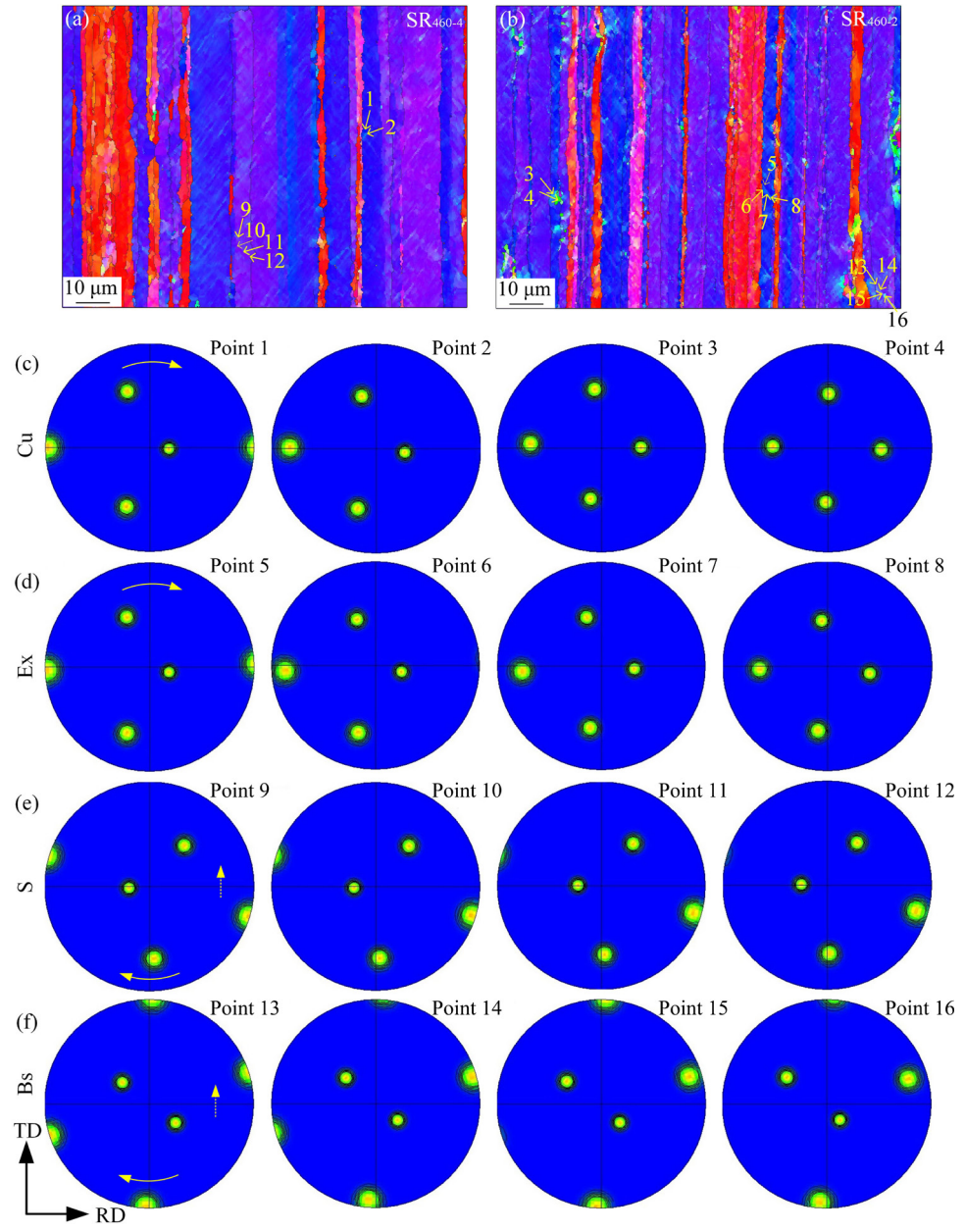


Fig. 14 Evolution of local orientation at shearing bands: (a, b) IPF maps of SR_{460-4} and SR_{460-2} samples; (c-f) Pole figures at Points 1-16 in (a, b)

Figure 14(c) displays pole figures of Points 1-4 at the shearing band in the Cu-oriented grains. The SR₄₆₀₋₂ sample, which experienced greater deformation, reflects the final transformation orientation of the shearing band. Therefore, Points 3 and 4 are selected from the SR₄₆₀₋₂ sample shown in Fig. 14(b). The initial ideal Cu $(1\overline{12})[1\overline{11}]$ orientation gradually rotates around the TD axis and transforms into the R-Cube(001)[110] orientation via the intermediate orientation of $(1\overline{14})[2\overline{2}\overline{1}]$. The local orientation evolution of the shearing bands in Ex-oriented grains is depicted in Fig. 14(d). As can be seen, the Ex orientation also mainly rotates around the TD axis and approaches to the R-Cube orientation, which is roughly consistent with that of the shearing band in the Cu-oriented grain. This suggests that the shearing bands in the grains with Cu and Ex orientations evolve towards the recrystallization orientation of the R-Cube. It can be inferred that the shearing band promotes the formation of new recrystallized grains through orientation rotation under sufficient deformation. The pole figures for Points 9-12 are displayed in Fig. 14(e). The orientation evolution at the shearing band in S-oriented grains primarily involves rotation around the TD axis, with a minor contribution from rotation around the RD axis. This rotation process causes the S(213)[364] orientation to transform to a recrystallized orientation of R(214)[121]. A similar evolution is observed in Bs-oriented grains, where the shearing band orientation also changes through rotation around both the TD and RD axes. The shearing band evolution also occurs in grains with Cube orientation, which is the same as the transformation process described in Section 3.3.3. That is, the transition from Cube to R-Goss is also achieved through rotation around the TD axis.

The above analysis supports the conclusion that the local orientation evolution at the shearing bands within grains of various orientations follows a consistent mode. This evolution primarily involves changing from the initial orientation to a new orientation around the TD axis. Additionally, grains with S or Bs orientations exhibit a minor rotation around the RD axis. The transformation of the shearing bands tends to produce various recrystallization orientations. Therefore, new recrystallized grains can be formed when the transformation is substantial.

4 Conclusions

- (1) Symmetric rolling leads to narrowing and fragmentation of the extrusion fiber grains, triggering geometric dynamic recrystallization. Intensive recrystallization and grain coarsening can be initiated at a rolling strain of 1.4–1.9, resulting in a weakened texture. The asymmetric rolling introduces greater shear strain than symmetric rolling, which further increases recrystallization degree and promotes the randomization of grain orientations.
- (2) The extrusion plate has a strong $\langle 111 \rangle$ fiber texture and is primarily composed of Ex $\{123\}\langle 111\}$ and Cu $\{112\}\langle 111\}$. During rolling deformation, the Ex and Cu components transform to the $S\{123\}\langle 634\rangle$ orientation. When subjected to large rolling deformation, the initial Bs{011}- $\langle 21\overline{1}\rangle$ texture evolves into R-Bs, S, and adjacent orientations. Additionally, the initial Cube {001}-(100) texture transforms towards R-Goss(011)- $\langle 011 \rangle$, but there is a high probability that the transformation terminates at a certain orientation in the evolution path. These orientation evolutions lead to the formation of new grains within the original extrusion fiber, finally causing the fragmentation and the geometric dynamic recrystallization of the fiber grains.
- (3) The shearing bands within grains with different orientations exhibit a consistent pattern of orientation evolution. This pattern primarily involves a rotation of the initial orientation around the TD axis to the recrystallization orientation. In grains with Ex and Cu orientations, the shearing bands transform towards R-Cube(001)[1 $\overline{10}$], whereas those in Cube grains change towards R-Goss (0 $\overline{11}$)[011]. Shearing bands in S grains evolve towards R (214)[$\overline{121}$].

CRediT authorship contribution statement

WANG: Yong-xiao Conceptualization, Investigation, Data curation, Formal analysis, Methodology, Writing - Original draft, Preparation, Funding acquisition; Yang FU: Writing - Review & editing; Xiao XU: Writing - Review & editing, Visualization, Validation, Supervision, Funding acquisition; Hui LI: Resources, Funding acquisition, Writing - Review & editing, Supervision; Wen-dong ZHANG: Investigation, Methodology, Instruments; Rui

FENG: Visualization, Validation, Software; **Yao-kun PAN:** Data curation, Resources; **Xiao-li CUI:** Visualization, Validation, Supervision.

Declaration of competing interest

The authors declare that they have no known competing financial interests or personal relationships that could have appeared to influence the work reported in this paper.

Data availability

The raw/processed data required to reproduce these findings cannot be shared at this time as the data also form part of an ongoing study.

Acknowledgments

This work was supported by the National Natural Science Foundation of China (No. 52205393), the Natural Science Foundation of Shandong Province, China (No. ZR2022QE263), the Science and Technology Commission of Shanghai Municipality, Shanghai Rising-Star Program, China (No. 23YF1413900), and the Science and Technology Innovation Plan of Shanghai Science and Technology Commission, China (Nos. 21010500800, 23010501100).

References

- [1] EL-ATY A A, XU Yong, GUO Xun-zhong, ZHANG Shi-hong, MA Yan, CHEN Da-yong. Strengthening mechanisms, deformation behavior, and anisotropic mechanical properties of Al–Li alloys: A review [J]. Journal of Advanced Research, 2018, 10: 49–67.
- [2] MENG Zi-jie, ZHANG Cun-sheng, WU Cheng-ge, ZHANG Hao, CHEN Liang, ZHAO Guo-qun, YAN Hai. Low cycle fatigue behavior and fatigue life prediction of 2195 Al–Li alloy at warm temperatures [J]. Transactions of Nonferrous Metals Society of China, 2023, 33: 2574–2587.
- [3] FU Rong, HUANG Yuan-chun, LIU Yu, LI Hui, WANG Zhi-wen. Influence of homogenization treatment on microstructure and recrystallization behavior of 2195 Al–Li alloy [J]. Transactions of Nonferrous Metals Society of China, 2023, 33: 2255–2271.
- [4] ZHAO Xin-yue, LIU Wen-sheng, XIAO Dai-hong, MA Yu-zhu, HUANG Lan-ping, TANG Ya. A critical review: Crystal structure, evolution and interaction mechanism with dislocations of nano precipitates in Al–Li alloys [J]. Materials & Design, 2022, 217: 110629.
- [5] WANG Yong-xiao, ZHAO Guo-qun. Hot extrusion processing of Al-Li alloy profiles and related issues: A review [J]. Chinese Journal of Mechanical Engineering, 2020, 33(1): 64.
- [6] LI Sha-sha, ZHAO Qi, LIU Zhi-yi, LI Fu-dong. A review of

- texture evolution mechanisms during deformation by rolling in aluminum alloys [J]. Journal of Materials Engineering and Performance, 2018, 27: 3350–3373.
- [7] LI Hao-ran, ZOU Zhi-tao, LI Jin-feng, XU Guo-fu, ZHENG Zi-qiao. Correlation between grain structures and tensile properties of Al–Li alloys [J]. Transactions of Nonferrous Metals Society of China, 2023, 33: 3597–3611.
- [8] WEN Feng, CHEN Ji-qiang, HAN Shuang, ZHOU Zi-xiang, ZHONG Shi-biao, ZHANG Ying-hui, LI Wei-rong, Guan Ren-guo. Effect of crystal orientations and precipitates on corrosion behavior of Al-Cu-Li single crystals [J]. Transactions of Nonferrous Metals Society of China, 2022, 32: 3887–3900.
- [9] HALES S J, HAFLEY R A. Texture and anisotropy in Al-Li alloy 2195 plate and near-net-shape extrusions [J]. Materials Science and Engineering A, 1998, 257: 153–164.
- [10] WANG Yong-xiao, ZHAO Guo-qun, XU Xiao, CHEN Xiao-xue. Effect of extrusion parameters on microstructure, texture and mechanical property anisotropy of spray deposited 2195 Al-Li alloy profile [J]. Materials Science and Engineering A, 2021, 818: 141406.
- [11] MA Yun-long, LI Jin-feng, ZHANG Run-zhe, TANG Jian-guo, HUANG Cheng, LI Hong-ying, ZHENG Zi-qiao. Strength and structure variation of 2195 Al-Li alloy caused by different deformation processes of hot extrusion and cold-rolling [J]. Transactions of Nonferrous Metals Society of China, 2020, 30: 835–849.
- [12] MAURICE C L, DRIVER J H. High temperature plane strain compression of cube oriented aluminium crystals [J]. Acta Metallurgica et Materialia, 1993, 41: 1653–1664.
- [13] VATNE H E, SHAHANI R, NES E. Deformation of cube-oriented grains and formation of recrystallized cube grains in a hot deformed commercial AlMgMn aluminium alloy [J]. Acta Materialia, 1996, 44: 4447–4462.
- [14] SURESH M, KALSAR R, MORE A M, BISHT A, NAYAN N, SUWAS S. Evolution of microstructure and texture in the third generation Al–Li alloy AA2195 during warm hybrid processing [J]. Journal of Alloys and Compounds, 2021, 855: 156750.
- [15] XIE Yuan-kang, DENG Yun-lai, WANG Yu, GUO Xiao-bin. Effect of asymmetric rolling and subsequent ageing on the microstructure, texture and mechanical properties of the Al-Cu-Li alloy [J]. Journal of Alloys and Compounds, 2020, 863: 155445.
- [16] JIN H, LLOYD D J. Evolution of texture in AA6111 aluminum alloy after asymmetric rolling with various velocity ratios between top and bottom rolls [J]. Materials Science and Engineering A, 2007, 465: 267–273.
- [17] HUANG Ke, LOGE R. A review of dynamic recrystallization phenomena in metallic materials [J]. Materials & Design, 2016, 111: 548-574.
- [18] RAKSHIT R, SARKAR A, PANDA S K, MANDAL S. Influence of out-of-plane stretch forming induced different strain paths on micro-texture evolution, slip system activity and Taylor factor distribution in Al-Li alloy [J]. Materials Science and Engineering A, 2022, 830: 142267.

- [19] WANG Xin-yun, SHEN Bo, DENG Lei, LI Jian-jun. Effects of original orientation combination on substructure characteristics during continuous dynamic recrystallization in an extruded Al-Cu-Li alloy [J]. Materials Characterization, 2017, 130: 113-122.
- [20] LIU Wen-chang, MORRIS J G. Texture evolution of polycrystalline AA5182 aluminum alloy with an initial {001}{110} texture during rolling [J]. Scripta Materialia, 2002, 47: 487–492.
- [21] LIU Wen-chang, MORRIS J G. Lattice rotation and stability of 22.5° ND rotated cube orientation in cold rolled polycrystalline AA5182 aluminum alloy [J]. Materials Science and Engineering A, 2004, 380: 147–154.
- [22] CHEN Yang, TIAN Ni, ZHAO Gang, LIU Chun-ming, ZUO Liang. Evolution of {001}⟨110⟩ orientation and related lattice rotation of Al alloy 6111 during rolling [J]. Transactions of Nonferrous Metals Society of China, 2007, 17: 523−530.
- [23] RAABE D, ZHAO Z, ROTERS F. Study on the orientational stability of cube-oriented FCC crystals under plane strain by use of a texture component crystal plasticity finite element method [J]. Scripta Materialia, 2004, 50: 1085–1090.
- [24] LIU Jian-tao, MORRIS J G. Macro-, micro- and mesotexture evolutions of continuous cast and direct chill cast AA3105 aluminum alloy during cold rolling [J]. Materials Science and Engineering A, 2003, 357: 277–296.
- [25] DONG Hai-ping, GUO Fei, HUANG Wei-jiu, YANG Xu-sheng, ZHU Xiang-hui, LI Hu, JIANG Lu-yang. Shear banding behavior of AA2099 Al–Li alloy in asymmetrical rolling and its effect on recrystallization in subsequent annealing [J]. Materials Characterization, 2021, 177: 111155.
- [26] YANG Yang, CHEN Ya-dong, JIANG Li-hong, LI Meng, ZHANG Qing-ming, TANG Tie-gang. Study on the characteristics and thermal stability of nanostructures in adiabatic shear band of 2195 Al–Li alloy [J]. Applied Physics A, 2015, 121: 1277–1284.
- [27] TANG Jia-guo, YI Yong-ping, HE Hai-lin, HUANG Shi-quan, ZHANG Jing-jing, DONG Fei. Hot deformation behavior and microstructural evolution of the Al-Cu-Li alloy: A study with processing map [J]. Journal of Alloys and Compounds, 2023, 934: 167755.
- [28] WANG Xiao-ya, JIANG Jian-tang, LI Guo-ai, WANG Xiao-ming, SHAO Wen-zhu, ZHEN Liang. Particle-stimulated nucleation and recrystallization texture initiated by coarsened Al₂CuLi phase in Al–Cu–Li alloy [J]. Journal of Materials Research and Technology, 2021, 10: 643–650.
- [29] LIN Ben, Ma Peng-cheng, LI Hao-ran, DENG San-xi, ZENG Guang-jun, TANG Jian-guo, LI Jin-feng, LI Xi-wu. Anisotropy of Al-Li alloy plate and its heredity effect in mechanical property distribution of spun-dome [J]. Transactions of Nonferrous Metals Society of China, 2023, 33: 1318-1330.
- [30] LI Hui, CHANG Cong, HUANG Yuan-chun, FU Rong, SHAO Hong-bang. Optimization of numerical parameters and microstructure evolution on 2195 Al–Li alloy extrusion process [J]. Journal of Materials Research and Technology,

[31] WANG Yong-xiao, ZHAO Guo-qun, XU Xiao, CHEN Xiao-xue, ZHANG Cun-sheng. Constitutive modeling, processing map establishment and microstructure analysis of

2023, 26: 7694-7706.

- processing map establishment and microstructure analysis of spray deposited Al–Cu–Li alloy 2195 [J]. Journal of Alloys and Compounds, 2019, 779: 735–751.
- [32] HORNBUCKLE B C, LUCKENBAUGH T L, FUDGER S J, ROBERTS A J, JANNOTTI P, BYUN T S, HOELZER D T, SOLANKI K, DARLING K A. Role of geometric dynamic recrystallization in nanocrystalline alloys [J]. Materialia, 2023, 30:101807.
- [33] HUMPHREYS F J, HATHERLY M. Recrystallization and related annealing phenomena [M]. 2nd ed. Amsterdam: Elsevier, 2004.
- [34] WANG Yong-xiao, ZHAO Guo-qun, CHEN Xiao-xue, XU Xiao, CHEN Liang, ZHANG Cun-sheng. Effect of interannealing between two stages of extrusion on the microstructure and mechanical property for spray deposited Al-Cu-Li alloy 2195 [J]. Journal of Materials Research and Technology, 2019, 8: 3891–3907.
- [35] GOURDET S, MONTHEILLET F. A model of continuous dynamic recrystallization [J]. Acta Materialia, 2003, 51: 2685–2699.
- [36] GAZIZOV M, MALOPHEYEV S, KAIBYSHEV R. The effect of second-phase particles on grain refinement during equal-channel angular pressing in an Al-Cu-Mg-Ag alloy [J]. Journal of Materials Science, 2015, 50: 990-1005.
- [37] LI Yi-bo, GU Bin, JIANG Shuai, LIU Yao-qiong, SHI Zhu-sheng, LIN Jian-guo. A CDRX-based material model for hot deformation of aluminium alloys [J]. International Journal of Plasticity, 2020, 134: 102844.
- [38] WANG Bing-feng, MA Rui, ZHOU Jin-dian, LI Ze-zhou, ZHAO Shi-teng, HUANG Xiao-xia. Adiabatic shear localization in ultrafine grained 6061aluminum alloy [J]. Materials Science and Engineering A, 2016, 675: 221–227.
- [39] WANG Shun-cai, STARINK M J, GAO Hong, QIAO Xiao-guang, XU Cheng, LANGDON T G. Texture evolution by shear on two planes during ECAP of a high-strength aluminum alloy [J]. Acta Materialia, 2008, 56: 3800–3809.
- [40] AZZEDDINE H, BAUDIN T, HELBERT A L, BRISSET F, HUANG Yi, KAWASAKI M, BRADAI D, LANGDON T G. A stored energy analysis of grains with shear texture orientations in Cu–Ni–Si and Fe–Ni alloys processed by high-pressure torsion [J]. Journal of Alloys and Compounds, 2021, 864: 158142.
- [41] GODFREY A, HANSEN N, JENSEN D J. Microstructural-based measurement of local stored energy variations in deformed metals [J]. Metallurgical and Materials Transactions A, 2007, 38: 2329–2339.
- [42] HIRSCH J, LÜCKE K. Mechanism of deformation and development of rolling textures in polycrystalline f.c.c. metals–II. Simulation and interpretation of experiments on the basis of Taylor-type theories [J]. Acta Metallurgica, 1988, 36: 2883–2904.
- [43] MAO Wei-min, YU Yong-ning. Reaction stress model and relaxation of reaction stress among the grains during tensile

- deformation of FCC metals [J]. Materials Science Forum, 2005, 495/496/497: 995–1000.
- [44] HIRSCH J, LÜCKE K. Mechanism of deformation and development of rolling textures in polycrystalline f.c.c. metals–I. Description of rolling texture development in
- homogeneous CuZn alloys [J]. Acta Metallurgica, 1988, 36: 2863–2882.
- [45] CHOWDHURY S G. Development of texture during cold rolling in AA5182 alloy [J]. Scripta Materialia, 2005, 52: 99–105.

2195 铝锂合金挤压和轧制加工中的织构演变

王永晓1.2, 付杨1,徐潇3,李辉1,张文东4,冯锐1,潘尧坤1,崔晓丽1

- 1. 山东理工大学 材料科学与工程学院,淄博 255000;
 - 2. 山东南山铝业股份有限公司, 龙口 265700;
 - 3. 上海电机学院 机械学院, 上海 201306;
 - 4. 临朐检验检测中心, 临朐 262600

摘 要:对 2195 铝锂合金进行挤压和轧制变形,研究该过程中显微组织和织构的演变行为。采用 EBSD 技术揭示了不同织构成分的微观演变机理。研究结果表明,织构演变存在两种机制:塑性应变引起的晶粒整体取向转变和晶内剪切带导致的局部取向转变。轧制变形时,Ex $\{123\}\langle11\overline{1}\rangle$ 和 Cu $\{112\}\langle11\overline{1}\rangle$ 挤压织构组分转变为 S $\{123\}\langle63\overline{4}\rangle$ 织构; Bs $\{011\}\langle21\overline{1}\rangle$ 织构组分则向 R-Bs 和 S 附近取向转变。随轧制变形量增加,S、Bs 和 R-Bs 组分绕 TD 轴旋转并散化成其他新取向,从而形成新的再结晶晶粒。具有不同初始取向的剪切带局部位置在轧制变形时其演变路径相似,均是由初始取向转变为一系列再结晶新取向。

关键词: 铝锂合金; 织构演变; 晶粒取向; 挤压和轧制加工; 显微组织

(Edited by Bing YANG)